for subsequent cases only includes this circularly polarized electric field input case for CGS.

Figures 4.36–4.38 present the photoelasticity and the vertical and horizontal shear CGS images. As expected, the fringe densities are smaller as compared to the larger $K_I = 0.514$ MPa$\sqrt{\text{m}}$ load case for photoelastic I_1 and I_2 in Figures 4.36(a) and 4.36(a) and for the CGS images in Figures 4.37 and 4.38. To reduce the noise source of the weak Fizeau fringes from the interference of the reflected light from the surfaces of the specimen, a Wiener filter with window size of $[25 \times 25]$ pixels is used on the photoelastic images before processing the data.

Before the presentation and discussion of the full-field data, Table 4.2 includes the RMSD values, experimental data ranges, and NRMSD values for the data for this load case. Overall, the global error (i.e., NRMSD) is low, ranging from 0.017 to 0.078, but higher for certain fields like $\sigma_1 + \sigma_2$, σ_{xx} and $\sigma_{\theta\theta}$ than for the larger $K_I = 0.514$ MPa$\sqrt{\text{m}}$ load case shown in Table 4.1. The higher NRMSD values are due to a smaller range of data; the RMSD values are comparable or even smaller for this smaller $K_I = 0.259$ MPa$\sqrt{\text{m}}$ load case. Unfortunately, for this case, $\sigma_{\theta\theta}$ has one of the highest errors, which diminishes confidence in the calculation of the constant of integration that uses $\sigma_{\theta\theta}$ along the crack, which may lead to some nominal propagated error in fields that utilize the $\sigma_1 + \sigma_2$ field. Here, σ_{xx} has the highest NRMSD value at 0.078, which is still overall remarkably low for data stemming from a hybrid experimental technique; most of the NRMSd values are under 0.05, which is quite low.

The photoelastic images are processed in the same manner as previously described with the correction of the wrapped isoclinic angle, the unwrapping of the isoclinic angle, the determination of the unambiguous wrapped isochromatic phase, the unwrapping of the isochromatic phase, and finally the determination of $\sigma_1 - \sigma_2$ field. The resulting photoelastic data, the isoclinic angle and the $\sigma_1 - \sigma_2$ fields shown in Figure 4.39, have similar features to the higher load case, where α has a radial symmetry and $\sigma_1 - \sigma_2$ is double lobed on either side of the crack tip. This lower load case has more apparent asymmetry about the crack plane due to the higher mode-mixity, seen in the larger rotation of the double lobes about the crack tip in the $-\theta$ direction. The experimental α again does not have the large change in value near $\theta = 0$ as found in the theoretical α, but exhibits

Quantity	Units	RMSD (in Units)	Data Range (in Units)	NRMSD (No Units)
α	rad.	0.17	7.10	0.025
$\partial(\sigma_1+\sigma_2)/\partial x$ from $\lambda/4$ plate method	MPa/mm	1.28	49.8	0.026
$\partial(\sigma_1+\sigma_2)/\partial y$ from $\lambda/4$ plate method	MPa/mm	1.81	52.3	0.035
$\sigma_1+\sigma_2$	MPa	0.70	12.2	0.058
$\sigma_1-\sigma_2$	MPa	0.15	8.83	0.017
σ_1	MPa	0.36	7.97	0.045
σ_2	MPa	0.34	6.28	0.055
σ_{xx}	MPa	0.47	6.05	0.078
σ_{yy}	MPa	0.39	8.16	0.036
σ_{xy}	MPa	0.17	6.41	0.026
σ_{rr}	MPa	0.30	8.69	0.034
$\sigma_{\theta\theta}$	MPa	0.44	5.68	0.077
$\sigma_{r\theta}$	MPa	0.24	5.43	0.044

Table 4.2: Error analysis for various experimental fields for specimen HomC1 for $K_I = 0.259$ MPa$\sqrt{\text{m}}$ and $K_{II} = 5.0$ kPa$\sqrt{\text{m}}$

a smoothing effect through this region that approximates the large change, evident in the line plot of the wrapped and unwrapped α for the experimental and theoretical data in Figure 4.39(c). This approximation is due to modulation of the wrapped α by the polarization optic misalignment error discussed in detail in Sections 3.2.1 and 4.2.4.2. The experimental $\sigma_1 - \sigma_2$ matches the theoretical data well evident by the small RMSD of only 0.15 MPa, which is mainly due to the larger load concentration near the crack tip in the theoretical field.

The experimental CGS data produce x and y derivatives of $\sigma_1 + \sigma_2$ that compare well with the theoretical derivatives, shown in Figure 4.40, except very close to the crack tip, which has higher stresses than the CGS method is likely to be able to detect with the shearing distance of 225 μm used for this case. The theoretical range of data for the x derivative is more than twice of the range captured by the experimental data, and the theoretical range for the y derivative is more than four times the experimental range. Though these observations are stark, they are misleading about the CGS data quality. Given a slightly larger mask around the crack tip with an added area of an annulus of radius $\sim$ 200 μm, the data ranges would agree well. Visually, the x derivative has the correct shape, and its values are mostly 25 MPa/mm or less as is the case for the theoretical data except very close to the tip. The theoretical y derivative data is mostly between -20 MPa/mm and 20 MPa/mm, which is true for the experimental data as well.

The asymmetry of the experimental $\sigma_1 + \sigma_2$ compares well with that of the theoretical $\sigma_1 + \sigma_2$ for $+x$ values, but the experimental field has a different asymmetry for $-x$ values, where the $(-x, +y)$ data points have a different curvature to the stress contour. This difference is most likely due to limitation of the CGS phases to represent derivatives of stress. Figure 4.41 reports the ϵ error maps due to the CGS assumption that the finite difference of $\sigma_1 + \sigma_2$ between two points divided by the distance between those points can represent the derivative of $\sigma_1 + \sigma_2$, as described above in Section 4.2.4.3. The error maps for pure Mode I loading, given in Figure 4.28, do not change for the same field of view and shearing distance, but the the addition of Mode II loading requires the calculation of these error maps for each individual case. Comparing the CGS error maps for the two load cases with $\mu_{SIF} = 0.0085$ and $\mu_{SIF} = 0.020$ in Figures 4.29 and 4.41, respectively, shows that the area with $\epsilon > 5\%$ is larger in the case with larger mode-mixity behind the crack in the vertical shearing direction, but the error maps for the horizontal shearing direction are similar for the two cases. These ϵ error maps do not show the actual error in the data, but show the regions where the data is more likely to be suspect. For example, the higher ϵ error behind the crack in the vertical shearing data corresponds to the greater difference between the experimental and theoretical $\sigma_1 + \sigma_2$. Despite these error predictions, the CGS data and related fields have reasonable NRMSD values.

The experimental and theoretical in-plane tensorial stresses have good agreement in form and stress concentration for most of the field. In Figure 4.42, the asymmetries due to the Mode II loading component are apparent in front of the crack in σ_1 and σ_2, the latter of which exhibits the sharp flame-like shape canted at an angle from $\theta = 0$ just as in the theoretical field. Due to errors from $\sigma_1 + \sigma_2$ behind the crack, σ_2 behind the crack does not agree as well with theory, especially for $(-x, +y)$ locations. In Figure 4.43, the experimental Cartesian stresses exhibit the expected form where σ_{xx} has a fish shape, σ_{yy} has a small kidney-bean shape, and σ_{xy} has a butterfly shape. The theoretical σ_{xx} has less asymmetry across the x axis just behind the crack than the experimental

σ_{xx} and a larger stress concentration, leading to the highest NRMSD error of 0.078 even though the RMSD is only 0.47 MPa. The theoretical σ_{yy} has a slightly higher stress concentration on the sides of the crack tip than the experimental field, and the experimental σ_{yy} for $(-x, +y)$ is different than predicted; yet, these differences only results in an NRMSD error of 0.036. The theoretical and experimental σ_{xy} compare extremely well with one of the lowest RMSD at 0.17 MPa and NRMSD at 0.026. The experimental polar stresses in Figure 4.44 have the correct form, but with local errors. The experimental σ_{rr} field more asymmetric behind the crack tip, but has low RMSD and NRMSD values. The experimental $\sigma_{\theta\theta}$ agrees well with theory in front of the crack, but not well behind the crack, leading to a a larger NRMSD at 0.077. The experimental $\sigma_{r\theta}$ does not compare well near the crack tip, most likely due to errors propagated from the isoclinic angle, but otherwise has good comparison with theory with average RMSD and NRMSD.

Line plots of the σ_{yy} stress along the crack plane, shown in Figure 4.45, are used to verify that the stress fields measured for this case are K-dominant stress fields that obey the 2D asymptotic crack solution. The experimental σ_{yy} in Figure 4.45(a) again is slightly lower than the theoretical, but the theoretical σ_{yy} is close to the RMSD bounds. The log-log plot of σ_{yy} versus r for $\theta = 0$ establishes the r dependence of the field, i.e., the experimental data fits the $-1/2$ slope, indicating that the data has the correct $1/\sqrt{r}$ behavior of a K-dominant stress field. The K dominance of the experimental stress allows for confident comparison of the experimental data with the the 2D asymptotic crack solution using the experimentally determined K_I and K_{II} values.

This lower load case for specimen HomC1 demonstrates that the hybrid CGS-photoelasticity method successfully determines the in-plane tensorial stress for a moderate load with K_I about half of the fracture toughness of Homalite-100. Stress determination at loading conditions significantly lower than the load condition required for crack propagation is necessary in fracture studies for monitoring of stress development, establishing the type of loading asymmetries and possible crack propagation directions in anisotropic materials. This lower load case, along with the higher load case, establishes that this experimental method is sensitive enough for determination of small Mode II contributions in Mode I–dominant stress fields, useful in future anisotropic material fracture studies.

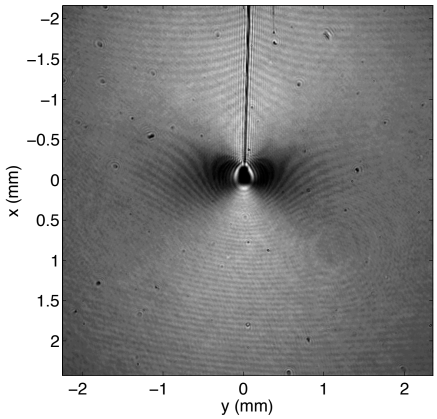

(a) $I_1 = I_o(1 + \cos(\delta))$

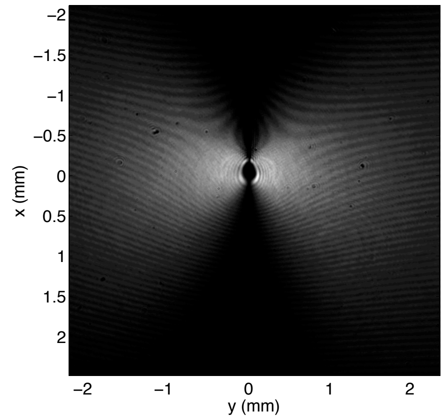

(b) $I_2 = I_o(1 - \cos(\delta))$

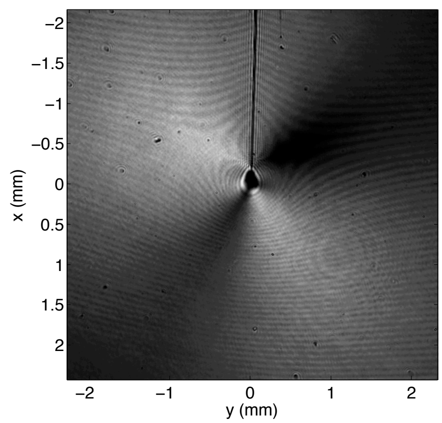

(c) $I_3 = I_o(1 - \sin(\delta)\sin(2\alpha))$

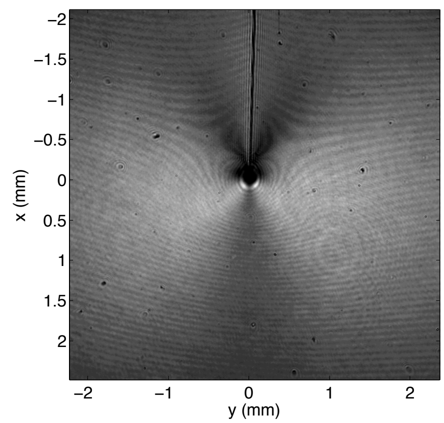

(d) $I_4 = I_o(1 + \sin(\delta)\cos(2\alpha))$

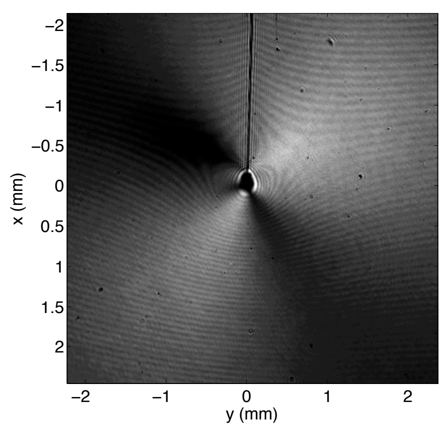

(e) $I_5 = I_o(1 + \sin(\delta)\sin(2\alpha))$

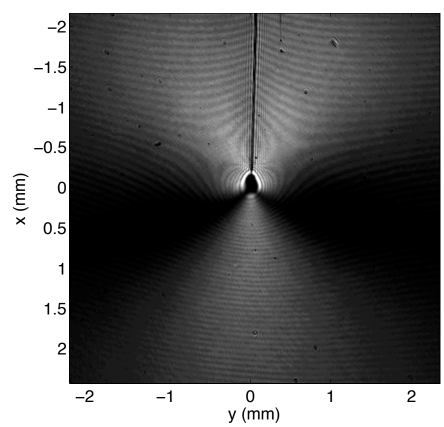

(f) $I_6 = I_o(1 - \sin(\delta)\cos(2\alpha))$

Figure 4.36: Experimental mages from six-step phase-shifting photoelasticity for specimen HomC1 for $K_I = 0.259$ MPa$\sqrt{\text{m}}$ and $K_{II} = 5.0$ kPa$\sqrt{\text{m}}$. Caustic shadows obscure the data at the crack tip due to the stress concentration, and the weak high density fringes overlaying the photoelastic fringes are due to the interference of the reflections from the front and back faces of the specimen.

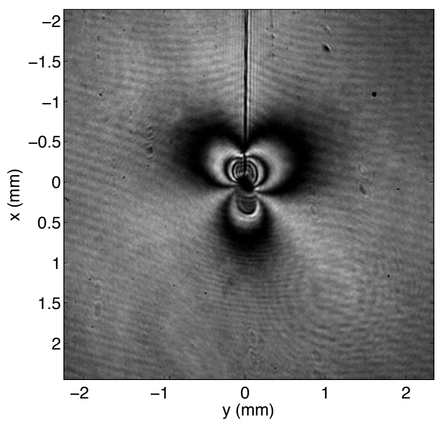

(a) I_1^{circ}

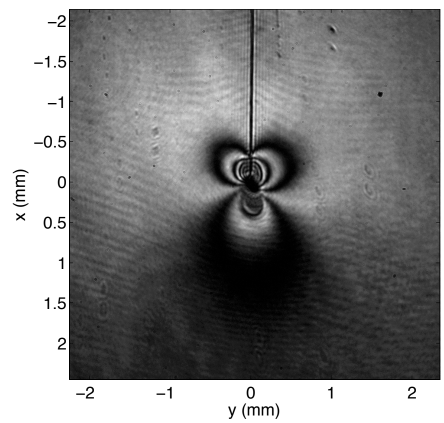

(b) I_2^{circ}

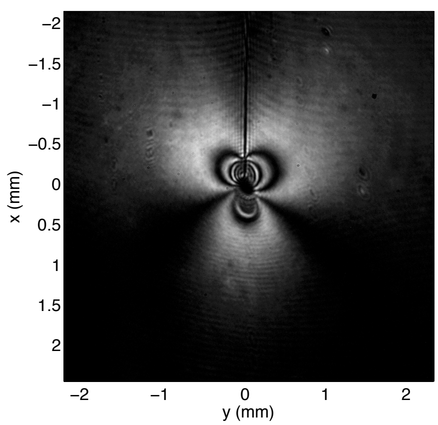

(c) I_3^{circ}

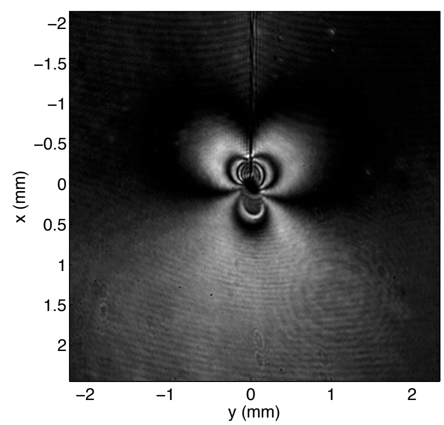

(d) I_4^{circ}

Figure 4.37: Experimental phase-shifted images from vertical shearing CGS using the $\lambda/4$ polarization method for specimen HomC1 for $K_I = 0.259$ MPa$\sqrt{\mathrm{m}}$ and $K_{II} = 5.0$ kPa$\sqrt{\mathrm{m}}$

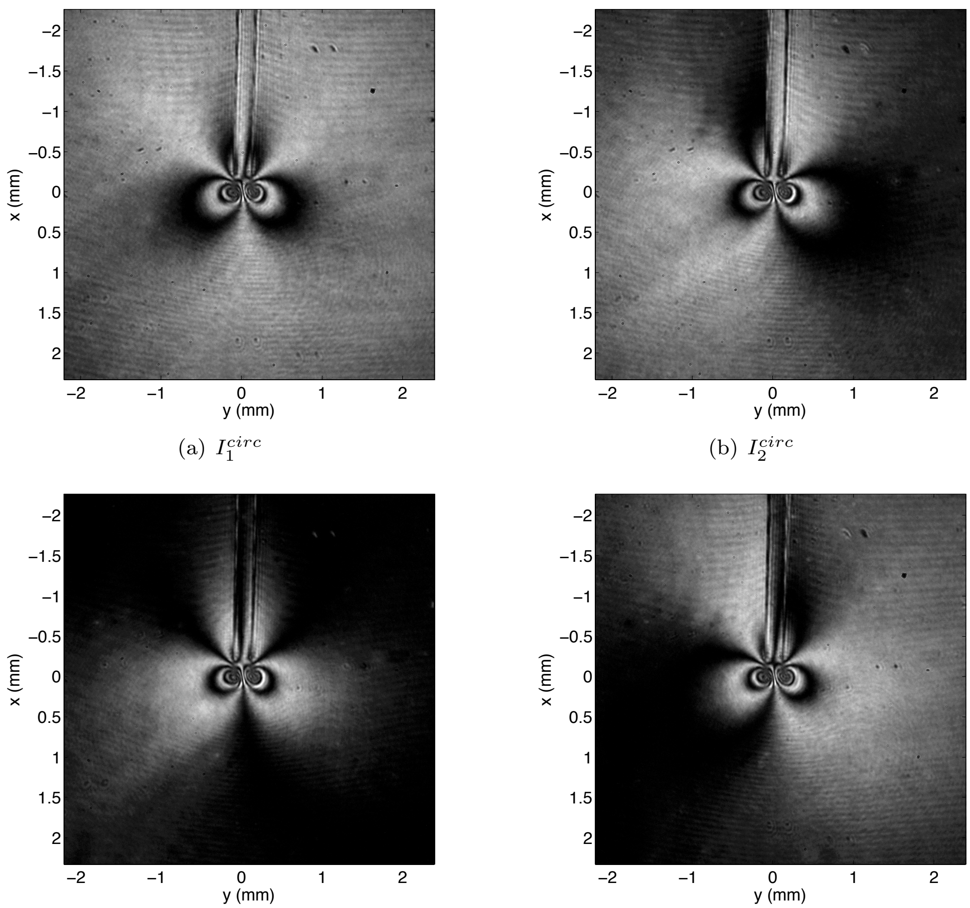

(a) I_1^{circ}

(b) I_2^{circ}

(c) I_3^{circ}

(d) I_4^{circ}

Figure 4.38: Experimental phase-shifted images from horizontal shearing CGS using the $\lambda/4$ polarization method for specimen HomC1 for $K_I = 0.259$ MPa$\sqrt{\text{m}}$ and $K_{II} = 5.0$ kPa$\sqrt{\text{m}}$

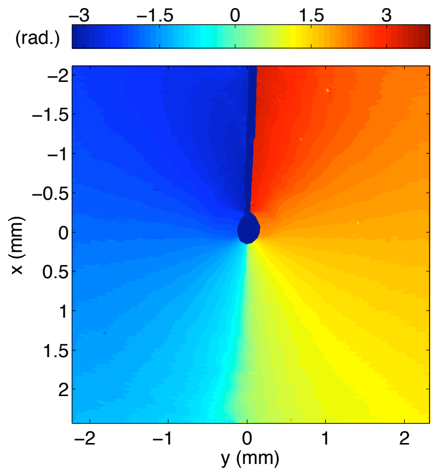

(a) Experimental unwrapped α

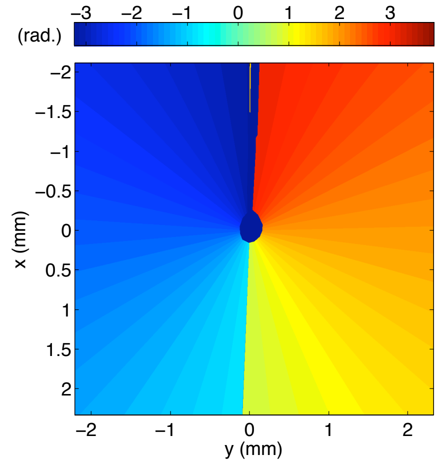

(b) Theoretical unwrapped α

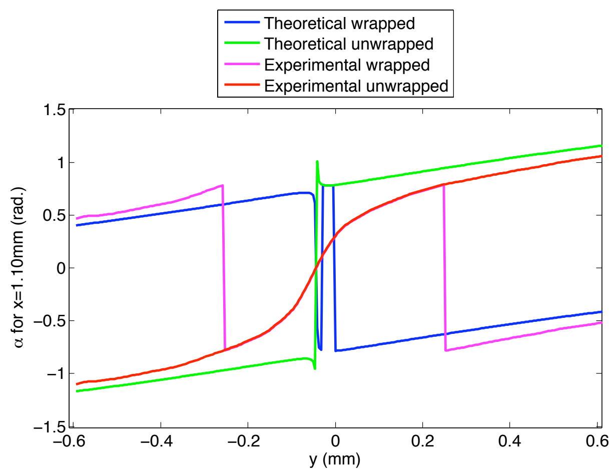

(c) Experimental and theoretical wrapped and unwrapped α

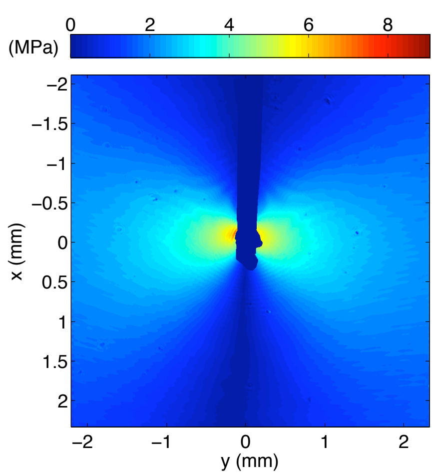

(d) Experimental $\sigma_1 - \sigma_2$

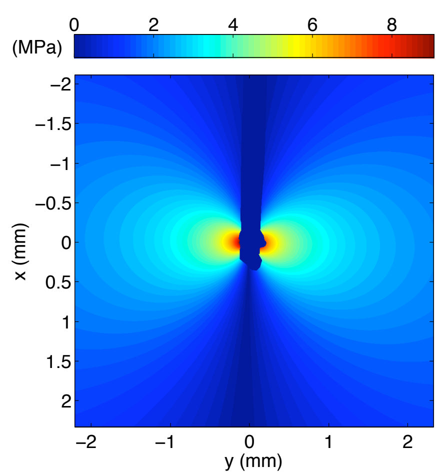

(e) Theoretical $\sigma_1 - \sigma_2$

Figure 4.39: Experimental and theoretical unwrapped α and $\sigma_1 - \sigma_2$ with crack region masked in blue and comparison of experimental and theoretical α for $x = 1.10$ mm